Optimal experimental design for joint reflection-transmission ultrasound breast imaging: From ray- to wave-based methods

Naiara Korta Martiartu, Christian Boehm, Vaclav Hapla, Hansruedi Maurer, Ivana Jovanović Balic, and Andreas Fichtner

Citation: The Journal of the Acoustical Society of America **146**, 1252 (2019); doi: 10.1121/1.5122291
View online: https://doi.org/10.1121/1.5122291
View Table of Contents: https://asa.scitation.org/toc/jas/146/2
Published by the Acoustical Society of America

Optimal experimental design for joint reflection-transmission ultrasound breast imaging: From ray- to wave-based methods

Naiara Korta Martiartu,[1,a)] Christian Boehm,[1] Vaclav Hapla,[1] Hansruedi Maurer,[1] Ivana Jovanović Balic,[2] and Andreas Fichtner[1]
[1]*Department of Earth Sciences, Eidgenössische Technische Hochschule Zürich, Zürich CH-8092, Switzerland*
[2]*SonoView Acoustic Sensing Technologies, Nidau CH-2560, Switzerland*

(Received 28 February 2019; revised 30 June 2019; accepted 30 July 2019; published online 21 August 2019)

Ultrasound computed tomography (USCT) is an emerging modality to image the acoustic properties of the breast tissue for cancer diagnosis. With the need of improving the diagnostic accuracy of USCT, while maintaining the cost low, recent research is mainly focused on improving (1) the reconstruction methods and (2) the acquisition systems. D-optimal sequential experimental design (D-SOED) offers a method to integrate these aspects into a common systematic framework. The transducer configuration is optimized to minimize the uncertainties in the estimated model parameters, and to reduce the time to solution by identifying redundancies in the data. This work presents a formulation to jointly optimize the experiment for transmission and reflection data and, in particular, to estimate the speed of sound and reflectivity of the tissue using either ray-based or wave-based imaging methods. Uncertainties in the parameters can be quantified by extracting properties of the posterior covariance operator, which is analytically computed by linearizing the forward problem with respect to the prior knowledge about parameters. D-SOED is first introduced by an illustrative toy example, and then applied to real data. This shows that the time to solution can be substantially reduced, without altering the final image, by selecting the most informative measurements. © *2019 Acoustical Society of America*. https://doi.org/10.1121/1.5122291

[BET] Pages: 1252–1264

I. INTRODUCTION

Ultrasound computer tomography (USCT) is a promising imaging technique for breast cancer screening. Ultrasonic waves are propagated through the tissue and recorded by a set of transducers that are surrounding the breast. The experiment collects transmission and reflection data, which are then used to obtain quantitative images of acoustic tissue properties. These properties, which include speed of sound, density, reflectivity, and attenuation, are useful for characterizing and classifying the breast tissue. In particular, they allow us to differentiate tumors from benign lesions (Greenleaf *et al.*, 1977; Stavros *et al.*, 1995).

In the last decade, USCT has emerged as an active field of research (Gemmeke and Ruiter, 2007; Ozmen *et al.*, 2015; Pérez-Liva *et al.*, 2017; Pratt *et al.*, 2007; Roy *et al.*, 2010; Sandhu *et al.*, 2015; Wiskin *et al.*, 2012). The main challenge addressed by the current studies is to provide a diagnostic tool with high accuracy (comparable to MRI) and affordable computational and acquisition cost for clinical practice (e.g., Ihrig and Schmitz, 2018; Matthews *et al.*, 2017; Taskin *et al.*, 2018; Wang *et al.*, 2014). This trade-off can be controlled by the choice of the reconstruction method as well as the setup of the scanning device. Addressing these aspects in a systematic manner will be the main focus of the present study.

Acoustic properties of the tissue are commonly reconstructed using ray-based approaches (Dapp *et al.*, 2011; Hormati *et al.*, 2010; Li *et al.*, 2009; Stotzka *et al.*, 2005). This includes, for instance, B-mode technique and time-of-flight tomography for reflection and transmission information, respectively. Based on the infinite-frequency approximation, they offer a valid solution for high frequency data (1–5 MHz), while being computationally efficient and robust. Whereas the B-mode can provide accurate reflection images, transmission images often suffer from limited spatial resolution. To improve this, tomographic methods relying on more accurate wave propagation models have been introduced (André *et al.*, 2013; Lavarello and Hesford, 2013). Among these techniques, waveform tomography methods have shown the most promising results in terms of spatial resolution and contrast (Goncharsky *et al.*, 2016; Ozmen *et al.*, 2015; Pratt *et al.*, 2007). However, new challenges arise: (1) The computational burden increases significantly with respect to ray-based approaches, especially for high frequencies or 3 D reconstructions and (2) the optimization problem becomes highly non-linear. Adapted acquisition systems that provide cost-effective designs and low-frequency data are therefore essential to both alleviate the cost and ensure meaningful solutions (Bunks *et al.*, 1995; Fichtner, 2010; Gauthier *et al.*, 1986).

During the last decade, several transducer setups have been investigated, ranging from circular to semi-ellipsoidal distributions (Camacho *et al.*, 2012; Duric *et al.*, 2014; Johnson *et al.*, 2007; Liu *et al.*, 2018; Ruiter *et al.*, 2012; Schwarzenberg *et al.*, 2007; Zografos *et al.*, 2013). Currently, the practical implementation of waveform tomography is limited to 2 D slice-by-slice scanning devices. Here, the cost of numerical wave propagation is reduced by 2 D approximations,

[a)]Electronic mail: naiara.korta@erdw.ethz.ch

which may, however, introduce undesirable artifacts in the reconstructions (Goncharsky *et al.*, 2016; Sandhu *et al.*, 2017; Wiskin *et al.*, 2013). Fully 3 D devices may overcome these limitations by including out-of-plane scattering and refraction. At present, however, high-frequency transducers are dominating such devices, which excludes the use of waveform tomography. Adapting the existing acquisition systems to new tomographic methods is not straightforward and opens new questions: What are the optimal acquisition designs, in terms of accuracy and cost, for each imaging method?

The studies above reveal an interdependency between (1) the quality of the reconstructed images, (2) the involved computational cost, (3) the applied tomographic method, and (4) the design of the experimental setup. To find an optimal trade-off between accuracy and cost, a framework that integrates these four aspects is key. In this sense, optimal experimental design (OED) methods offer a powerful tool, and they have been successfully applied to similar problems, for instance, in seismic exploration (Curtis *et al.*, 2004; Guest and Curtis, 2009; Maurer *et al.*, 2010, 2017). The goal of OED is to optimize the experimental setup in order to maximize the information about the region of interest (ROI) that can be retrieved from the observations. In addition, OED methods provide benefit-cost curves that quantify the information gain versus the computational cost related to different experimental configurations. These curves are particularly useful to identify redundancies in the measurements, and by doing so, maximize the benefit-cost ratio of an experiment (Maurer *et al.*, 2017).

Methods to optimally design the experimental setup have been recently introduced in USCT (Gemmeke *et al.*, 2014; Korta Martiartu *et al.*, 2017; Maurer *et al.*, 2017; Vinard *et al.*, 2018). They have been formulated either for time-of-flight inversion using straight rays or for time-domain waveform inversion. In other words, these formulations account only for transmission information. An optimal scanning system, however, should simultaneously provide accurate results for both transmission (e.g., speed of sound) and reflection (reflectivity) information. The main objective of this work is to present a general OED formulation for joint optimizations, in which the experimental setup is optimized, in terms of accuracy and cost, to image both reflection and transmission information. Our approach not only collects the tomographic methods already introduced by previous studies, but also extends to reflectivity imaging techniques. Therefore, we consider both the conventional ray-based and the most advanced wave-based imaging methods.

The rest of the paper is organized as follows. We first present the theoretical aspects of the OED problem. Using the Bayesian approach, we formulate the quality of an experimental design in terms of the uncertainties in the parameters that we expect post-reconstruction. Naturally, the quality measure will depend on the specific imaging method applied, and we therefore introduce the explicit expressions for four imaging approaches. Next, we illustrate the performance of our OED approach using a numerical toy example, and we conclude by applying it to real data.

II. OPTIMAL EXPERIMENTAL DESIGN METHOD

A. Bayesian inverse problem

The goal of USCT is to estimate the acoustic tissue parameters $\mathbf{m}$ from the observations of the ultrasound signals $\mathbf{d}_{\text{obs}}$ that are recorded by an experimental setup $\mathbf{s}$. For instance, $\mathbf{m}$ represents the distribution of the speed of sound in space; $\mathbf{d}_{\text{obs}}$ contains the recorded times of the first arrivals; and $\mathbf{s}$ denotes the locations of the active transducers on the scanning device.

The physical model that predicts observable parameters $\mathbf{d}$ from model parameters $\mathbf{m}$ can be expressed by the forward operator $\mathbf{F}$ as

$$\mathbf{d} = \mathbf{F}(\mathbf{m};\mathbf{s}) + \boldsymbol{\epsilon}, \tag{1}$$

where the vector $\boldsymbol{\epsilon}$ accounts for the measurement noise that we assume to be Gaussian with zero-mean and covariance matrix $\boldsymbol{\Gamma}_{\text{noise}}$. In Secs. III A and III B, we discuss specific formulations for the forward operator that approximate the ultrasonic wave propagation with different degrees of accuracy.

In USCT, the non-linearities of $\mathbf{F}(\mathbf{m};\mathbf{s})$ with respect to $\mathbf{m}$ are not too severe in the context of OED. In particular, we assume that the acoustical parameters show relatively small variations with respect to some prior knowledge $\mathbf{m}_{\text{prior}}$. This can be, for instance, the medium in which calibration data is recorded. In such situations, we can linearize the forward operator as

$$\mathbf{F}(\mathbf{m};\mathbf{s}) \approx \mathbf{F}(\mathbf{m}_{\text{prior}};\mathbf{s}) + \mathbf{F}'(\mathbf{m};\mathbf{s})|_{\mathbf{m}=\mathbf{m}_{\text{prior}}}(\mathbf{m}-\mathbf{m}_{\text{prior}}), \tag{2}$$

where higher-order model perturbation terms have been neglected. Here, $\mathbf{F}'$ is the first derivative of the forward operator with respect to $\mathbf{m}$, i.e., the Jacobian operator. For notational simplicity, we will continue using $\mathbf{F}'(\mathbf{s})$ to express $\mathbf{F}'(\mathbf{m};\mathbf{s})$ evaluated at $\mathbf{m}_{\text{prior}}$.

Measurement noise, limited data coverage, and the approximations in the forward operator introduce uncertainties into the estimated parameters. From Bayesian inference theory, the solution to the inverse problem is therefore described as the *posterior* probability density function $\pi(\mathbf{m}|\mathbf{d};\mathbf{s})$, which combines the data likelihood and our prior beliefs about the parameters. For simplicity, we assume the latter to be Gaussian, with mean $\mathbf{m}_{\text{prior}}$ and covariance matrix $\boldsymbol{\Gamma}_{\text{prior}}$. This aspect will be further discussed in Sec. II D.

For the forward problem in Eq. (2), the posterior $\pi(\mathbf{m}|\mathbf{d};\mathbf{s})$ is also Gaussian (Tarantola, 2005),

$$\pi(\mathbf{m}|\mathbf{d};\mathbf{s}) \propto \exp\left[-\frac{1}{2}\left(\Delta\mathbf{m}-\widetilde{\Delta\mathbf{m}}\right)^T\boldsymbol{\Gamma}_{\text{post}}^{-1}\left(\Delta\mathbf{m}-\widetilde{\Delta\mathbf{m}}\right)\right], \tag{3}$$

with mean

$$\widetilde{\Delta\mathbf{m}} = \boldsymbol{\Gamma}_{\text{post}}(\mathbf{s})\mathbf{F}'(\mathbf{s})^T\boldsymbol{\Gamma}_{\text{noise}}^{-1}\Delta\mathbf{d}_{\text{obs}} \tag{4}$$

and posterior covariance matrix

$$\boldsymbol{\Gamma}_{\text{post}}(\mathbf{s}) = \left(\mathbf{F}'(\mathbf{s})^T \boldsymbol{\Gamma}_{\text{noise}}^{-1} \mathbf{F}'(\mathbf{s}) + \boldsymbol{\Gamma}_{\text{prior}}^{-1}\right)^{-1}. \tag{5}$$

Here, we denote $\Delta\mathbf{d}_{\text{obs}} = \mathbf{d}_{\text{obs}} - \mathbf{F}(\mathbf{m}_{\text{prior}}; \mathbf{s})$ and $\Delta\mathbf{m} = \mathbf{m} - \mathbf{m}_{\text{prior}}$. The weighted norms are defined as $||\mathbf{x}||^2_{\Gamma^{-1}} = \mathbf{x}^T\boldsymbol{\Gamma}^{-1}\mathbf{x}$, where the superscript T represents the transpose operation of a vector or matrix.

The term $\mathbf{F}'(\mathbf{s})^T\boldsymbol{\Gamma}_{\text{noise}}^{-1}\mathbf{F}'(\mathbf{s})$ in the posterior covariance matrix $\boldsymbol{\Gamma}_{\text{post}}(\mathbf{s})$ is the data misfit Hessian (Attia *et al.*, 2018), and it shows useful properties to measure the quality of an experimental configuration. First, it depends on the parameters that define the experimental setup. This allows us to compare different candidates and select the ones that give the lowest uncertainties in the parameter estimation. Second, it neither depends on the observations nor the unknown model parameters, which means that it could be used to optimize the experiment before any realization. Last, it shows the same structure for any forward operator, under the condition that these are linear or can be linearized with respect to the model parameters. This allows us to present general formulations of the OED problem, independent of the tomographic method that is intended to be applied post-acquisition.

1. Joint posterior covariance

Ideally, an experimental setup should be flexible enough to provide reliable reconstructions of different acoustic parameters using multiple tomographic methods. Assume, for instance, that we expect to reconstruct the speed of sound $\mathbf{m}_1$ and the reflectivity $\mathbf{m}_2$ of the tissue using the imaging techniques $\mathbf{F}_1$ and $\mathbf{F}_2$, respectively. Moreover, we denote by $\mathbf{d}_1$ and $\boldsymbol{d}_2$ the corresponding observed data, and by $\boldsymbol{\Gamma}_1$ and $\boldsymbol{\Gamma}_2$ the covariance matrix of the noise for each case, respectively. We can formulate the joint forward problem as

$$\begin{bmatrix}\Delta\mathbf{d}_1\\ \Delta\mathbf{d}_2\end{bmatrix} = \begin{bmatrix}\mathbf{F}'_1 & \mathbf{0}\\ \mathbf{0} & \mathbf{F}'_2\end{bmatrix}\begin{bmatrix}\Delta\mathbf{m}_1\\ \Delta\mathbf{m}_2\end{bmatrix}, \tag{6}$$

which essentially consists of two separable subproblems. Here we have simplified the notation as $\mathbf{F}'_i = \mathbf{F}'_i(\mathbf{s})$ for clarity. If we now define $\Delta\mathbf{d}_{\text{obs}} = [\Delta\mathbf{d}_1; \Delta\mathbf{d}_2]$ and $\Delta\mathbf{m} = [\Delta\mathbf{m}_1; \Delta\mathbf{m}_2]$, and we denote the joint forward operator as $\mathbf{F}'$, the posterior covariance matrix will be given by Eq. (5). In this case, the data misfit Hessian is a block-diagonal matrix,

$$\begin{aligned}\mathbf{H}_{\text{misfit}}(\mathbf{s}) = \mathbf{F}'^T\boldsymbol{\Gamma}^{-1}\mathbf{F}' &= \begin{bmatrix}\mathbf{F}_1'^T\boldsymbol{\Gamma}_1^{-1}\mathbf{F}'_1 & \mathbf{0}\\ \mathbf{0} & \mathbf{F}_2'^T\boldsymbol{\Gamma}_2^{-1}\mathbf{F}'_2\end{bmatrix}\\ &= \begin{bmatrix}\mathbf{H}_{\text{misfit},1} & \mathbf{0}\\ \mathbf{0} & \mathbf{H}_{\text{misfit},2}\end{bmatrix},\end{aligned} \tag{7}$$

with $\boldsymbol{\Gamma}^{-1}$ being a block-diagonal matrix composed by $\boldsymbol{\Gamma}_1$ and $\boldsymbol{\Gamma}_2$.

As a first approximation, our formulation neglects the trade-offs between parameter $\mathbf{m}_1$ and $\mathbf{m}_2$, which is justified by the specific nature of each subproblem. This point will be further discussed in Sec. III C.

B. Quality measure

Our ability to invert $\mathbf{H}_{\text{misfit}}$ will determine how the uncertainties in the data space are mapped into the model parameters. For example, small eigenvalues of the matrix will yield large variances in the model parameters, which translates to higher uncertainty in the reconstruction. Assume that Θ is a scalar function that quantifies the level of expected uncertainties in the parameters by extracting some properties from $\mathbf{H}_{\text{misfit}}$. Then, we can formulate the OED problem as a minimization problem,

$$\min_{\mathbf{s}\in\mathcal{S}} \Theta(\mathbf{H}_{\text{misfit}}(\mathbf{s})), \tag{8}$$

where $\mathcal{S}$ represents the space for all possible experimental configurations.

There are various definitions for Θ that have been successfully applied in the field of OED (Curtis, 2004; Khodja *et al.*, 2010). The use of different design criteria mostly depends on the involved computational complexity for the specific problem under consideration. In this study, we consider the D-optimality condition (Alexanderian and Saibaba, 2018; Atkinson and Donev, 1992; Attia *et al.*, 2018), which defines Θ as

$$\Theta = \log\det(\boldsymbol{\Gamma}_{\text{post}}) = -\log\det\left(\mathbf{H}_{\text{misfit}} + \boldsymbol{\Gamma}_{\text{prior}}^{-1}\right). \tag{9}$$

One can compute this quantity using Cholesky factorization of $\mathbf{H}_{\text{misfit}} + \boldsymbol{\Gamma}_{\text{prior}}^{-1}$, which is positive definite by construction. Note that $\boldsymbol{\Gamma}_{\text{prior}}^{-1}$ acts as a threshold for small eigenvalues of $\mathbf{H}_{\text{misfit}}$. We can alleviate the cost of computing Θ by reducing the domain to a subset of parameters. This is particularly helpful to maximize the information about a specific ROI.

The determinant corresponds to the product of the eigenvalues, and thus, the D-optimal design minimizes the volume of the uncertainty ellipsoid in the estimated parameters. From information theory, this quantity can be related to the expected information gain Ψ (Attia *et al.*, 2018), which is an important property for our application. We compute this by subtracting from Θ the contribution of the prior $\boldsymbol{\Gamma}_{\text{prior}}$, i.e., $\Psi = -\Theta + \log\det(\boldsymbol{\Gamma}_{\text{prior}})$. Furthermore, the D-optimal designs show invariant properties with respect to different model reparameterizations (Dette and O'Brien, 1999). This may be crucial when the parameterization for the reconstructions is not known beforehand. Here, we refer to the discretization of the acoustic tissue parameters as parameterization.

For joint optimizations introduced in Sec. II A 1, the quality measure is the combination of terms related to each subproblem,

$$\begin{aligned}\Theta = &-\log\det\left(\mathbf{H}_{\text{misfit},1} + \boldsymbol{\Gamma}_{\text{prior},1}^{-1}\right)\\ &- \log\det\left(\mathbf{H}_{\text{misfit},2} + \boldsymbol{\Gamma}_{\text{prior},2}^{-1}\right).\end{aligned} \tag{10}$$

Note that the data and prior covariances weigh the contribution of both terms. We further discuss this aspect in Sec. IV.

C. Sequential optimal experimental design

Our ultimate goal is to optimize the measurements collected from USCT acquisition systems using Eq. (8). This can be controlled, for instance, by the number and locations of the transducers on the device. A common strategy is to predefine the total number N of candidate locations for the transducers, and to define the experimental design $\mathbf{s}$ as an array of binary entries that selects a subset of them: 0 for nonactive transducers, and 1 for the active ones. Although this approach reduces significantly the design space $\mathcal{S}$, it still includes all transducer combinations, the total number being $\sum_{i=1}^{N}\binom{N}{i} = 2^N - 1$, and it may become very large for problems with a large number of design parameters N.

To make the optimization problem computationally tractable, we aplpy the sequential optimal experimental design (SOED) method (Guest and Curtis, 2009; Maurer *et al.*, 2010). In this approach, we start from an experimental configuration that considers all candidate transducers active, and we deactivate them one by one in each iteration. The overall algorithm describing our implementation of the SOED method is given in Algorithm 1. Here, we denote by $\mathbf{s}_k = (s_1, \ldots, s_N) \in \{0,1\}^N$ the transducer configuration found at the k-th iteration. Our method samples a total number of $N(N+1)/2$ experimental designs.

ALGORITHM 1: Algorithm for SOED method.

1: Consider all candidate transducers active: $\mathbf{s}_0 = (1, \ldots, 1)$.
2: **while** $\mathbf{s}_k$ has at least one active transducer **do**
3: **for** $i \leftarrow 1$ to n **do** ▷ n: number of active transducers in $\mathbf{s}_k$.
4: Deactivate i-th transducer.
5: Compute and store Θ for the remaining configuration.
6: Deactivate from $\mathbf{s}_k$ the transducer that minimizes Θ.

Due to the sequential nature of the algorithm, SOED has the advantage of providing benefit-cost curves. An example of this is shown in Fig. 1. They illustrate the gain in the data information content with respect to the experimental cost (Maurer *et al.*, 2017). They are particularly useful maximize the benefit-cost ratio of the experiment by identifying redundancies in the observations. In Sec. IV, we further discuss these curves using a toy example.

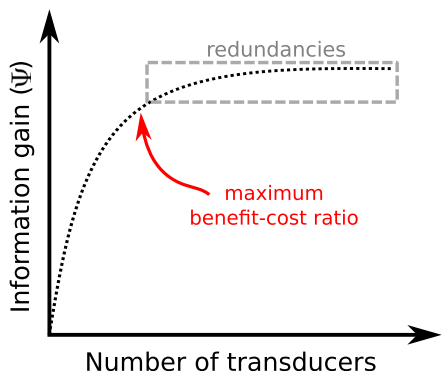

FIG. 1. (Color online) Illustrative example of the benefit-cost curve obtained from SOED approach.

D. Non-Gaussian priors

While non-Gaussian priors are often used in USCT (Li *et al.*, 2009; Matthews *et al.*, 2017), in this study we rely on Gaussian priors to formulate the D-optimal SOED (D-SOED) approach. In this way, analytical expressions of the posterior are available [see Eq. (5)]. To compute the D-optimality criterion, (1) we constrain the model parameters to the ROI, (2) we assume equally reliable observations, $\mathbf{\Gamma}_{\text{noise}} = \sigma_n \mathbf{I}$, and (3) we define $\mathbf{\Gamma}_{\text{prior}} = \sigma_p \mathbf{I}$, σ_p^{-1} being small enough to stabilize the inversion of the ill-conditioned matrix $\mathbf{H}_{\text{misfit}}$. As a result, our algorithm selects the experimental designs improving most the properties of $\mathbf{H}_{\text{misfit}}$. In particular, we expect the optimal designs to improve the effective rank of $\mathbf{H}_{\text{misfit}}$, which has a rapidly decaying spectrum. Because the regularization techniques mainly act in the effective nullspace of $\mathbf{H}_{\text{misfit}}$, reconstruction algorithms that use other priors will also benefit from our solutions.

III. APPLICATION TO IMAGING TECHNIQUES

The D-SOED strategy outlined above may be applied to any linearizable inverse problem. Here we specifically focus on four imaging methods considered for USCT, and we provide the respective Jacobian operators. All these methods approximate the acoustic wave equation

$$\frac{1}{\rho(\mathbf{x})c^2(\mathbf{x})}\partial_t^2 p(\mathbf{x},t) - \nabla\cdot\left(\frac{1}{\rho(\mathbf{x})}\nabla p(t,\mathbf{x})\right) = \frac{1}{\rho(\mathbf{x})} f(t,\mathbf{x}_s) \tag{11}$$

with different degree of accuracy. Here, p is the acoustic pressure field, and f is the external source generated from emitting transducers at $\mathbf{x}_s$. The parameters ρ and c represent the density and speed-of-sound distributions, respectively. Because in this study we do not consider imaging techniques that reconstruct the density distribution, we assume this as a constant in our derivations. The model parameters to estimate are therefore the speed of sound $c(\mathbf{x})$ and the reflectivity $I(\mathbf{x}) = 2\delta c(\mathbf{x})/c_0$, c_0 and $\delta c(\mathbf{x})$ being the background speed of sound and the perturbations with respect to it, respectively. These parameters are retrieved from the observations of the pressure field $p(\mathbf{x}_r, t; \mathbf{x}_s)$ at receiver positions $\mathbf{x}_r$, and in particular, we extract the information of the first-arrival times $T(\mathbf{x}_s, \mathbf{x}_r)$ and the scattered wavefields $\delta p(\mathbf{x}_r, t; \mathbf{x}_s)$. Linking to the notation used to formulate the joint forward problem in Eq. (6), we denote the unknown parameters as $\Delta\mathbf{m} = [\Delta\mathbf{m}_1; \Delta\mathbf{m}_2] = [\delta c(\mathbf{x}); I(\mathbf{x})]$, and the observed data as $\Delta\mathbf{d}_{\text{obs}} = [\Delta\mathbf{d}_1; \Delta\mathbf{d}_2] = [\delta T(\mathbf{x}_s, \mathbf{x}_r); \delta p(\mathbf{x}_r, t; \mathbf{x}_s)]$.

A. Ray-based methods: Infinite-frequency

1. Time-of-flight straight-ray tomography: Speed of sound

For the speed-of-sound reconstructions, first-arrival times are often approximated by straight-ray models (Dapp *et al.*, 2011; Li *et al.*, 2009). Here, changes in the time of

flight $\delta T(\mathbf{x}_s^i, \mathbf{x}_r^i)$ of the i-th ray that travels from the emitter at $\mathbf{x}_s^i$ to the receiver at $\mathbf{x}_r^i$ are related to the speed-of-sound perturbations as

$$\delta T(\mathbf{x}_s^i, \mathbf{x}_r^i) = -\int_{\text{ray}_i} \frac{\delta c(\mathbf{x}(l))}{c_0^2} dl \approx \sum_{j=1}^{N} \frac{l_{ij}}{c_0^2} \Delta c_j, \tag{12}$$

where $\mathbf{x}(l)$ is position along the ray-path in terms of arclength l. In the discrete form, we assume that the ROI has been partitioned into N cells with constant speed of sound. Then, l_{ij} represents the length of the i-th ray in the j-th cell, Δc_j being the corresponding speed-of-sound difference with respect to c_0. If the experiment has collected a total of M measurements, the Jacobian operator is a matrix of size $M \times N$ with the elements given by

$$\mathbf{F}'_{ij} = \frac{l_{ij}}{c_0^2}. \tag{13}$$

2. B-mode technique: Reflectivity

The B-mode technique is widely used to image the reflectivity of breast tissue. Based on the delay-and-sum principle, the image is constructed by focusing the received energy into the scatterer locations. The method assumes single-scattering, and computes the times of flight T using straight rays, similar to Eq. (12). The imaging condition for the reflectivity distribution $I(\mathbf{x})$ is

$$I(\mathbf{x}) = \sum_s \sum_r E(\mathbf{x}_r, t = T(\mathbf{x}_s, \mathbf{x}) + T(\mathbf{x}, \mathbf{x}_r); \mathbf{x}_s), \tag{14}$$

where E is the envelope of the recorded signal $p(\mathbf{x}_r, t; \mathbf{x}_s)$. The summation over s and r indicates all emitter-receiver combinations. Each time instant of the recorded signal is transformed to a space location using the emitter-scatterer-receiver geometry, where each grid point is a possible scatterer location.

Equation (14) approximates the unknown reflectivity distribution, and it is a proxy to the solution of the underlying inverse problem. To obtain more accurate images, different studies have reformulated Eq. (14) into a forward and inverse problem (Lavarello *et al.*, 2006). In the context of optimal design, we expect equivalent solutions for both approaches. In the following, we derive the forward problem of the B-mode technique.

We first assume an unbounded homogeneous medium with speed of sound c_0. For a point source $f(t)\delta(\mathbf{x} - \mathbf{x}_s)$, the pressure field $p_0(\mathbf{x}, t)$ is analytically expressed as

$$p_0(\mathbf{x}, t) = \frac{1}{4\pi||\mathbf{x} - \mathbf{x}_s||} f\left(t - \frac{||\mathbf{x} - \mathbf{x}_s||}{c_0}\right), \tag{15}$$

where $||\mathbf{x} - \mathbf{x}_s||$ is the Euclidean distance between $\mathbf{x}$ and $\mathbf{x}_s$.

Now, assume that the medium is slightly perturbed to $c_0 + \delta c(\mathbf{x})$. The new wavefield can be expressed as $p_0 + \delta p$, where δp is the scattered field due to the perturbation δc. Under the Born approximation, the acoustic wave equation that relates δp and δc is given by

$$\left(\frac{1}{c_0^2}\partial_t^2 - \nabla^2\right)\delta p(\mathbf{x}, t) = \frac{2\delta c(\mathbf{x})}{c_0^3}\partial_t^2 p_0(\mathbf{x}, t). \tag{16}$$

The scattered field δp is generated by secondary sources exited due to the interaction of the pressure field p_0 with the perturbation δc. Similar to Eq. (15), the solution can be expressed as (Tarantola, 1984)

$$\begin{aligned}\delta p(\mathbf{x}, t) = &\frac{1}{16\pi^2 c_0^2}\int_V \frac{1}{||\mathbf{x} - \mathbf{x}'||||\mathbf{x}' - \mathbf{x}_s||}\delta \\ &\times \left(t - \frac{||\mathbf{x} - \mathbf{x}'|| + ||\mathbf{x}' - \mathbf{x}_s||}{c_0}\right) \\ &\times I(\mathbf{x}')d\mathbf{x}' * \partial_t^2 f(t),\end{aligned} \tag{17}$$

where V is the volume of the ROI and * indicates the convolution operation. This equation describes the forward problem related to the B-mode imaging. Typically, to obtain sharper reflectivity images, the source-time function is deconvolved from the measured signals, and the transmitted information is muted from them. We denote as $[t_0, t_1]$ the time interval of the scattered information in the recorded signals, being t_1 the recording length. Therefore, for the measurement i that combines the emitter $\mathbf{x}_s$ and the receiver $\mathbf{x}_r$, the elements of the discrete Jacobian are

$$\mathbf{F}'_{ij} = \frac{1}{16\pi^2 c_0^2}\Delta V_j \frac{1}{||\mathbf{x}_r - \mathbf{x}_j||||\mathbf{x}_j - \mathbf{x}_s||}\delta_{[t_0,t_1]}(\tau_j), \tag{18}$$

where ΔV_j is the volume of the j-th cell located at $\mathbf{x}_j$, and

$$\delta_{[t_0,t_1]}(\tau_j) = \begin{cases} 1, & \tau_j \in [t_0, t_1] \\ 0, & \tau_j \notin [t_0, t_1] \end{cases} \quad \text{with} \quad \tau_j = \frac{||\mathbf{x}_r - \mathbf{x}_j|| + ||\mathbf{x}_j - \mathbf{x}_s||}{c_0}. \tag{19}$$

B. Wave-based methods: Finite-frequency

Ultrasonic sources used in USCT are band-limited, and finite-frequency effects may be important. Recently, wave equation based approaches have been proposed to improve the resolution of the USCT images. These include waveform tomography for speed-of-sound reconstructions (Boehm *et al.*, 2018; Matthews *et al.*, 2017; Pérez-Liva *et al.*, 2017; Pratt *et al.*, 2007) and reverse-time migration (RTM) for reflectivity images (Roy *et al.*, 2016).

1. Time-of-flight waveform tomography: Speed of sound

Waveform inversion is often stated as a non-linear least-squares problem, in which we minimize the L_2-distance between the observed and modelled signals (Boehm *et al.*, 2018; Goncharsky *et al.*, 2016; Roy *et al.*, 2010). Waveform differences, however, are highly non-linear with respect to the model parameters, and convergence towards the global minimum may be difficult. In seismic tomography, a variety of misfit functionals with improved convexity have been proposed (Bozdag *et al.*, 2011; Fichtner *et al.*, 2008; Luo and Schuster, 1991; Warner and Guasch, 2016). In this

study, we consider the cross-correlation time-of-flight misfit functional (Luo and Schuster, 1991; Marquering *et al.*, 1999), which quantifies the differences between predicted and measured first-arrival times. In contrast to waveform differences, the non-linearities of times of flight with respect to the speed-of-sound perturbations are weak, and it justifies the linearized assumptions introduced in Sec. II A (Mercerat and Nolet, 2012).

Assume that $T(\mathbf{x}_s^i, \mathbf{x}_r^i)$ is the time-of-flight difference between the observed and modelled signal (in c_0) computed from the cross-correlations. Anomalies in the time-of-flight difference are related to the speed-of-sound perturbations through the finite-frequency sensitivity kernel $K(\mathbf{x}; \mathbf{x}_r^i, \mathbf{x}_s^i)$ as (Korta Martiartu *et al.*, 2019; Luo and Schuster, 1991)

$$\delta T_i = \int_V K(\mathbf{x}; \mathbf{x}_r^i, \mathbf{x}_s^i) \delta c(\mathbf{x}) d\mathbf{x}. \tag{20}$$

Here, the volume V represents the ROI. The sensitivity kernel is given by

$$\begin{aligned} K(\mathbf{x}; \mathbf{x}_r^i, \mathbf{x}_s^i) &= K^i(\mathbf{x}) \\ &= -\frac{2}{c_0^3(\mathbf{x})} \int_0^{t_1} \partial_t p_0(\mathbf{x}, t; \mathbf{x}_s^i) \partial_t p_0^\dagger(\mathbf{x}, t_1 - t; \mathbf{x}_r^i) dt, \end{aligned} \tag{21}$$

where $[0,\ t_1]$ is the time interval in which the first arrivals occur. $p_0(\mathbf{x}, t; \mathbf{x}_s^i)$ is the pressure field propagated through c_0 due to the emitter at $\mathbf{x}_s^i$, and $p_0^\dagger(\mathbf{x}, t_1 - t; \mathbf{x}_r^i)$ is the backpropagated pressure field from the receiver at $\mathbf{x}_r^i$. The dagger symbol represents the adjoint field derived from the cross-correlations (Luo and Schuster, 1991; Tromp *et al.*, 2005).

Equation (20) describes the linearized forward problem for the time-of-flight waveform tomography. In the discrete form, the Jacobian matrix is computed as

$$\mathbf{F}'_{ij} = K^i(\mathbf{x}_j) \Delta V_j, \tag{22}$$

where $\mathbf{x}_j$ and ΔV_j are the position and the volume of the j-th cell, respectively.

2. Reverse-time migration: Reflectivity

RTM has recently been introduced to USCT to image the reflectivity distribution of the breast tissue (Roy *et al.*, 2016). The standard imaging condition $I(\mathbf{x})$ is based on the cross-correlation between the wavefield $p(\mathbf{x}, t; \mathbf{x}_s)$ propagated forward in time from emitters at $\mathbf{x}_s$, and the time-reversed measured wavefield $p^\dagger(\mathbf{x}, t_1 - t; \mathbf{x}_r)$ propagated from the receivers at $\mathbf{x}_r$ (Claerbout, 1971; Dai and Schuster, 2013),

$$I(\mathbf{x}) = \sum_s \int_0^{t_1} \partial_t^2 p(\mathbf{x}, t; \mathbf{x}_s) p^\dagger(\mathbf{x}, t_1 - t; \mathbf{x}_r) dt. \tag{23}$$

The sum over s stacks the contributions from all emitters.

Similar to B-mode imaging, RTM is based on the Born approximation of the acoustic wave equation [Eq. (16)]. The background speed-of-sound model $c_0(\mathbf{x})$ is the solution to the time-of-flight (waveform) tomography. Hence, the perturbed wavefield $\delta p(\mathbf{x}, t)$ related to the speed-of-sound anomaly δc is computed as

$$\begin{aligned} \delta p(\mathbf{x}, t) = \int_V \frac{I(\mathbf{x}')}{c_0^2(\mathbf{x}')} G_0(\mathbf{x}, t; \mathbf{x}', 0) \\ * \left[G_0(\mathbf{x}', t; \mathbf{x}_s, 0) * \partial_t^2 f(\mathbf{x}_s, t) \right] d\mathbf{x}', \end{aligned} \tag{24}$$

where $G_0(\mathbf{x}, t; \mathbf{x}_s, 0)$ represents the Green's function of the model $c_0(\mathbf{x})$ due to a source at $\mathbf{x}_s$. Because of the heterogeneous background model, the Green's functions are computed by numerical simulations of wave propagation, which is the main difference between RTM and B-mode [see Eqs. (24) and (17)].

If we linearize the forward problem using the prior information $c_0(\mathbf{x}) = c_0$, we obtain the same forward operator as in B-mode imaging. We therefore expect that, an optimized experimental configuration for B-mode, will also be optimized for RTM.

C. Sensitivities in the Jacobian operator

Figure 2 illustrates the information encoded in a row of the Jacobian $\mathbf{F}'$ for each imaging technique discussed above. By definition, each row represents how sensitive a single measurement is to changes in the model parameters.

For transmission data in the infinite-frequency approximation, times of flight are only sensitive to changes in the model parameters along the geometrical ray path [Fig. 2(a)]. When we incorporate finite-frequency effects, sensitivities extend away from the ray paths, showing an ellipsoidal shape defined by the Fresnel zones. Figures 2(b) and 2(c) show two examples with frequencies in the range of 0.2–0.8 MHz and 1–3 MHz, respectively. The sensitivity along the ray path is low in magnitude (Marquering *et al.*, 1999), especially observed at lower frequencies. At high frequencies, the sensitivity kernel becomes narrower, consistent with what ray theory predicts. We expect these differences to affect the optimized experimental designs in each case.

For reflection data, Figs. 2(d) and 2(e) show the sensitivities of the scattered signal to perturbations in the model parameters. These examples use the sources corresponding to the frequency ranges discussed above. The sensitivity corresponds to the time-space transformation ellipsoid multiplied by a term that accounts for spherical divergence effects [see Eq. (18)]. The size of the sensitive area is the result of the signal duration (0.14 ms) and frequencies. The lack of sensitivity in the interior of the ellipsoid is due to the direct arrivals, which are muted to include only the scattered information. For lower frequencies, the zero-sensitivity area is larger due to the longer period of the direct arrivals. Finite-frequency tomography sensitivities in Figs. 2(b) and 2(c) are complementary to the reflection sensitivities. Tomography resolves the low-wavenumber components of the medium, whereas the high wavenumbers are obtained by reflection imaging (migration) (Mora, 1989). An experimental setup therefore should be optimal to jointly retrieve transmission-reflection information from the measurements, which is the main focus of this paper.

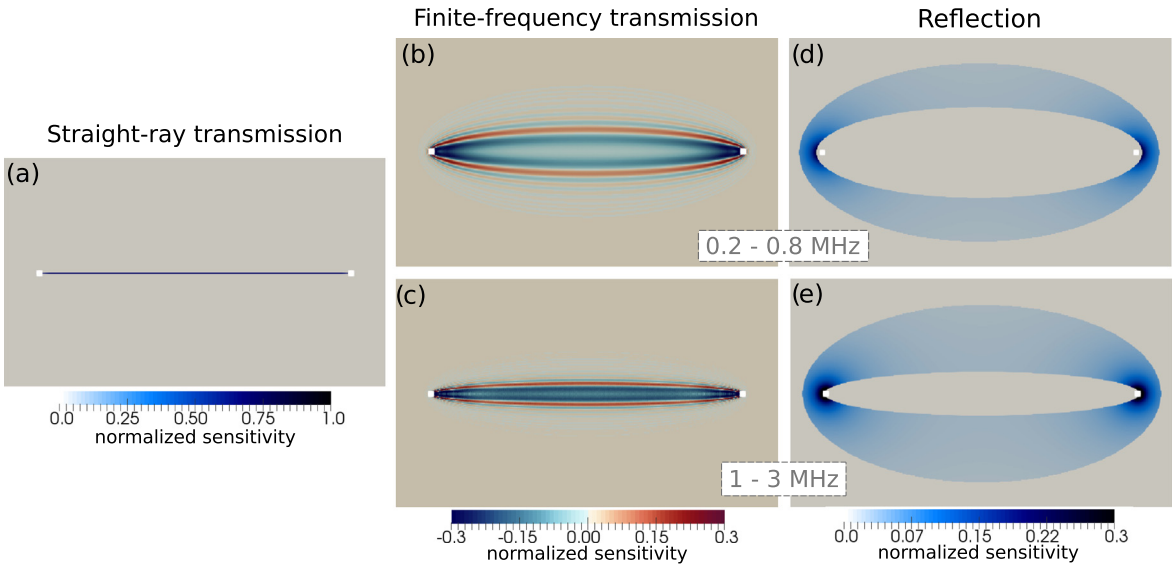

FIG. 2. (Color online) Normalized sensitivity to model parameters encoded in the Jacobian operator of a single measurement. (a) Time-of-flight tomography using straight rays. (b), (c) Time-of-flight waveform tomography using a broad-band pulse of 0.2–0.8 MHz and 1–3 MHz, respectively. (d), (e) Reflection imaging technique, with direct arrivals muted, corresponding to the sources in (b) and (c), respectively. The white dots indicate the emitter-receiver locations.

In the following we illustrate the potential of the joint D-SOED approach, first using an intuitive toy example, and then with an application to real data provided by CSIC/USM as part of the *USCT Data Challenge 2017* (Ruiter *et al.*, 2017).

IV. TOY EXAMPLE

In our toy example, we consider a circular configuration of radius 10 cm with 125 regularly spaced transducers, shown in Fig. 3. Here, we only take one transducer as emitter (red dot), and the rest as receivers (white dots). The source signal is a broad-band pulse, with frequencies in the range 350 kHz–1.2 MHz, and the recording time length is 0.14 ms. The unknown parameters are discretized on a rectilinear grid of 1 mm. Because our D-SOED algorithm does not depend on the model parameters, we only specify a ROI in which we want to minimize the uncertainties. In the interest of producing intuitively interpretable results, we define a relatively small ROI, indicated by the white circle of radius 1.5 cm.

Our goal is to apply D-SOED to identify the most informative receivers when recording both transmission and reflection data. First, we analyze the sensitivity of our acquisition system to the ROI. This will allow us to gain deeper insight into the relationship between the experimental design and the individual imaging methods. Second, we optimize the receiver configuration separately for each imaging technique. We use this to introduce the D-SOED algorithm and to discuss the benefit-cost curves described in Sec. II C. Finally, we perform the joint transmission-reflection optimization of the experimental design.

A. Sensitivity of the acquisition system

To understand the information that our acquisition system can exploit from each imaging technique, we first illustrate in Fig. 3 the stacked sensitivities to model parameters of all emitter-receiver combinations, which can be interpreted as sensitivity coverage.

Figure 3(a) shows the sensitivity coverage for the time-of-flight tomography with straight rays. Only few receivers facing the emitter collect signals that contain information about the ROI, which in fact is very sparse. We therefore

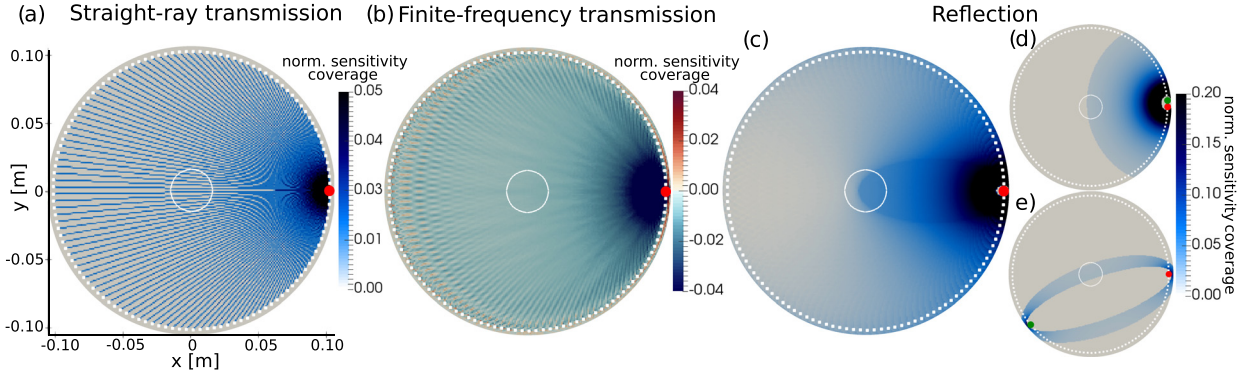

FIG. 3. (Color online) Normalized sensitivity coverages for a circular configuration with 125 transducers. The white circle indicates the ROI, and the red and white dots are the emitter and receivers, respectively. (a) Time-of-flight tomography using straight rays. (b) Time-of-flight waveform tomography using a broad-band pulse of 350 kHz–1.2 MHz. (c) Reflection imaging technique. (d), (e) Two examples of single measurement sensitivities for reflection data. Here, the green dots indicate the active receivers.

expect that the D-SOED algorithm will select these receivers as the most informative ones, giving a steep benefit-cost curve.

For finite-frequency tomography the information about the ROI is more uniform, as shown in Fig. 3(b). Compared to Fig. 3(a), receivers located at larger angles are also sensitive to the ROI. We therefore expect that the D-SOED algorithm will identify a larger number of informative receivers.

Figure 3(c) displays the sensitivity coverage for the reflection imaging technique. To understand this better, we moreover show in Figs. 3(d) and 3(e) two examples of single measurements for receivers located on the reflection- and transmission-side, respectively. Both types of measurements are sensitive to the ROI, and the combination of both will cover the entire ROI. We therefore expect the D-SOED algorithm to select receivers at both sides, with even more density on the transmission-side due to the sparse information collected from there. Though this may initially appear counterintuitive, it is an effect of the recording time length, the location and size of the ROI, and the circular configuration of transducers.

B. Individual optimizations

We apply the D-SOED algorithm separately for each imaging technique. The resulting benefit-cost curves are shown in Fig. 4(a). In all cases the information gain increases monotonically with the number of receivers, which means that more measurements improve the estimation of the parameters. At a certain point, however, the curves become flat. This occurs when the experiment includes receivers that either do not collect any information about the ROI or introduce redundancies. The transition between both stages, and in particular the point with the maximum curvature, represents the optimal benefit-cost ratio for the experiment, indicated by dashed lines in Fig. 4(a).

Receiver configurations with the optimal benefit-cost ratio are displayed in Figs. 4(b)–4(d). All results show the expected features discussed in Sec. IV A. Because our ultimate goal is the joint optimization, we focus on comparing the optimized setups for transmission and reflection data. On the one hand, we do not observe any receiver that was simultaneously selected as the most informative one for transmission with straight rays and reflection. Indeed, the uninformative receivers for reflection data (identified in the flat part of the benefit-cost curve) are the most informative ones for tomography with straight rays. We therefore expect that the joint optimization between these two techniques will result in the superposition of both individual optimizations. On the other hand, when we consider finite-frequency tomography, there is an overlap between the most informative receivers for reflection and transmission. Here we expect that the D-SOED algorithm will select first the receivers in common for both imaging techniques. Due to this overlap, in the following we use the latter combination of techniques to discuss the joint D-SOED algorithm.

C. Joint optimization

We apply the D-SOED algorithm using the joint forward formulation in Eq. (6) for finite-frequency tomography and reflection imaging. Figure 5(a) displays joint and individual benefit-cost curves for transmission and reflection, revealing three stages of the algorithm. Sensitivity coverages for each stage are shown in Figs. 5(b)–5(g). First, the algorithm selects receivers that are simultaneously sensitive to the ROI for both transmission and reflection. Consequently, both individual benefit-cost curves increase with the number of receivers. Then, receivers informative only for the transmission technique are selected. The corresponding information gain increases while remaining almost constant for reflection data. Finally, the experimental design is completed with receivers on the reflection-side, which are uniquely informative through the reflection technique. Here, the transmission benefit-cost curve remains constant, and it increases monotonically for the reflection. During all these stages the joint information gain increases monotonically.

The data and prior covariances weigh the contribution of each imaging technique in the joint optimization. Different choices will mostly affect the order in which the D-SOED algorithm selects the poorly informative receivers for each imaging technique. In our toy example, if the reflection technique contributes stronger to Θ in Eq. (10), the receivers facing the emitter will be selected last. In other words, this would affect the second and third stages illustrated in Fig. 5. However, we do not expect significant differences in the first stage, in which the algorithm selects first the receivers that contribute most for both techniques. Due to the nature of the determinant, the D-SOED algorithm

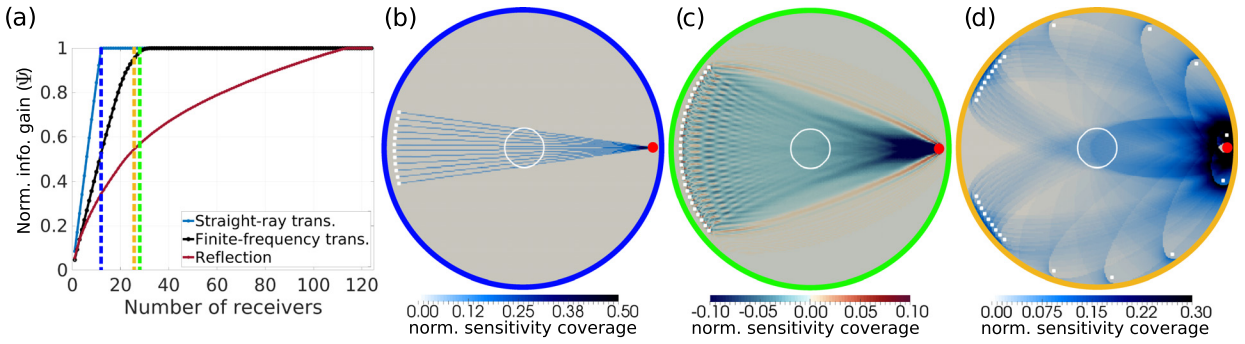

FIG. 4. (Color online) Results from D-SOED method applied to each imaging technique. (a) Benefit-cost curves representing the information gain Ψ with respect to the number of receivers. The dashed lines indicate the respective optimal number of receivers. (b)–(d) Normalized sensitivity coverages for the experiments using the most informative receivers obtained in each case: (b) time-of-flight tomography using straight rays (12 receivers), (c) time-of-flight waveform tomography (28 receivers), and (d) reflection imaging technique (26 receivers). The outlined circles link (b) and (c) to the dashed lines in (a).

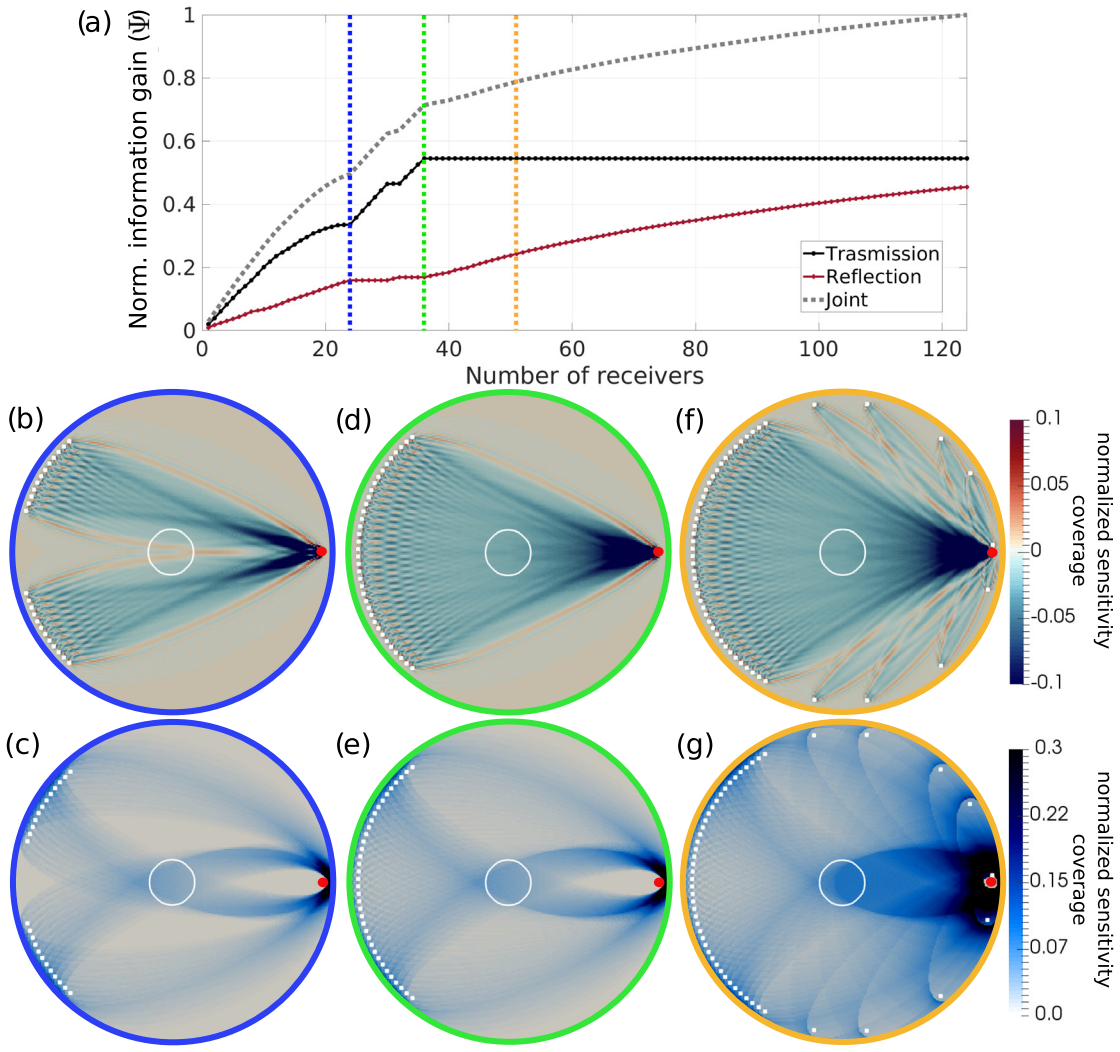

FIG. 5. (Color online) Results from joint transmission-reflection D-SOED algorithm. (a) Joint and individual benefit-cost curves for each imaging technique. The curves are normalized by the total joint information gain Ψ. Blue (left), green (middle), and yellow (right) dashed lines indicate 24, 36, and 51 (the optimal) number of receivers, respectively. (b), (d), (f) Transmission and (c), (e), (g) reflection sensitivity coverages for the optimized configurations with 24, 36, and 51 receivers, respectively.

essentially finds compromises between the parameters, providing solutions with balanced information.

V. REAL DATA APPLICATION: EMITTER SELECTION

To validate our algorithm, we apply the D-SOED method to real data. We consider the dataset provided as part of the *SPIE USCT Data Challenge 2017* by the Spanish National Research Council (CISC) and the Complutense University of Madrid (UCM). The dataset contains 64 768 A-scans recorded from a setup that consists of two transducer arrays of 16 elements. The transducers in one array act as emitters, with dominant frequency of 3.5 MHz, whereas the ones in the other array are recording. For each position of the emitting array, the receiving array is placed in 11 different positions, as shown in Fig. 6, and the whole system is rotated into 23 different positions, describing a circle with radius 95 mm. The main data coverage is obtained in a circular ROI of radius 7 cm. The true model used in this experiment is a phantom based on water, gelatine, graphite powder, and alcohol, and it is illustrated in Fig. 6. It has a cylindrical homogeneous background with a diameter of 94 mm, two inclusions of 2 cm diameter, and two steel needles (Camacho *et al.*, 2012; Ruiter *et al.*, 2018).

In this application, our goal is to decrease the data volume to reduce the time to solution. Here, the number of measurements is mainly controlled by the total number of emitting elements in the transducer array. Each element adds $23 \times 176 = 4048$ new measurements to the dataset. We therefore aim to select the most informative ones, removing those that provide redundant information about the ROI. This choice of the design parameter has an additional main reason: for imaging techniques based on numerical wave propagation (e.g., RTM or waveform tomography), the computational cost is proportional to the number of wave propagation simulations, and this is related to the number of emitters.

We apply the D-SOED method to jointly optimize the emitter configurations for transmission and reflection, using both straight-ray and finite-frequency transmission techniques. As in the example before, we parameterize the model

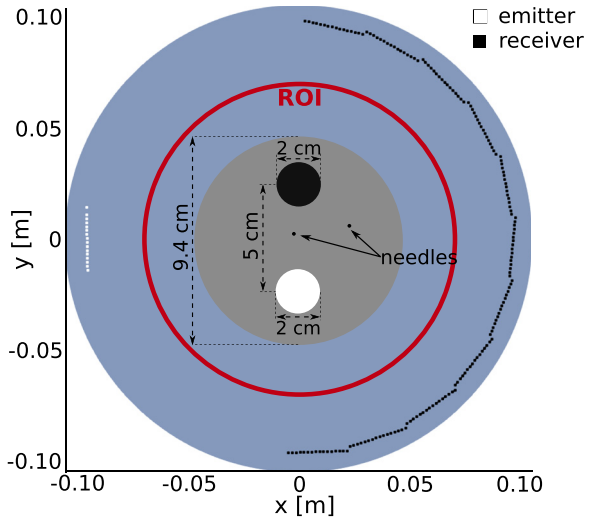

FIG. 6. (Color online) The acquisition system and phantom used to collect the CSIC/UCM dataset. The circle in red indicates the ROI considered for this study, which has a radius of 7 cm. White and black dots outside the ROI represent the transducers in the emitting and receiving array (in 11 different positions), respectively. An illustration of the true model is shown inside the ROI.

using a rectilinear grid with 1 mm mesh size. The benefit-cost curves are shown in Fig. 7(a). In both curves the optimal benefit-cost ratio is reached for four emitters. This may be an effect of the relatively high frequencies used in the experiment, in which the finite-frequency sensitivities become closer to ray-based predictions. For a fixed number of emitters, the curves moreover show how the information gain varies for randomly selected emitter locations. In this application, the choice of the emitter locations has a less significant effect on the information gain than the number of emitters. This is due to the good data coverage provided by the aperture, in general, and by not reducing the number of receivers during the D-SOED, in particular. Despite the small variations, our D-SOED algorithm certainly selects solutions close to the optimal in each case.

To verify our interpretation of the benefit-cost curves, we compare the reconstructions obtained from the optimized setups with the ones obtained using all emitters. For transmission tomography, we apply total variation regularization (Jensen *et al.*, 2012), and the results are shown in Figs. 7(b)–7(e). Our reconstructions are in agreement with the results obtained by other studies (Ruiter *et al.*, 2018). For both imaging techniques, reconstructions using only 25% of the dataset are almost identical to the ones using the complete dataset. The root-mean-square error (RMSE), comparing the observed times of flight with the times of flight predicted by the reconstruction, is indicated in the figures. In all cases, we compute the RMSE using the complete dataset, showing that the results from optimized setups explain the data equally well. This means that, effectively, our D-optimal algorithm accurately identifies the redundancies in the measurements. The supplementary material[1] also includes reconstructions at different stages of the benefit-cost curves.

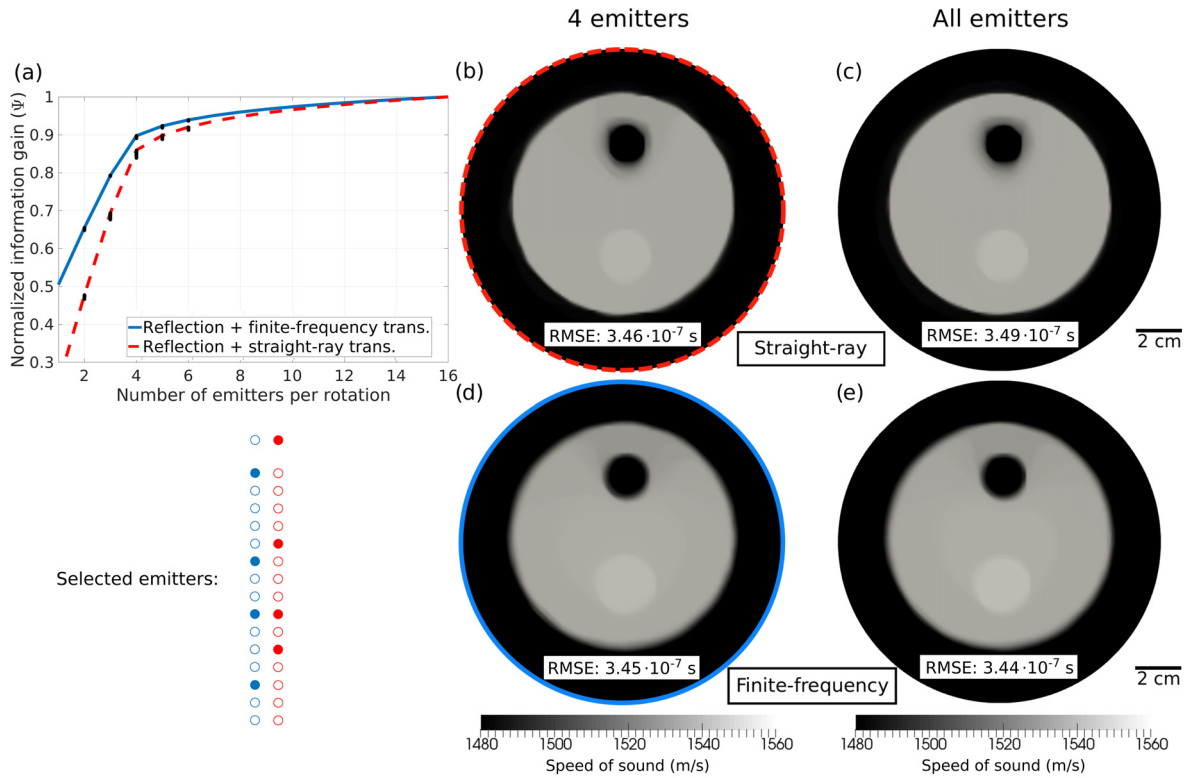

FIG. 7. (Color online) (a) Benefit-cost curves of D-SOED for reflection-transmission when considering straight-rays (red dashed line) and finite-frequencies (blue solid line). For 2 to 6 number of emitters, black lines indicate the variation in the information gain Ψ for randomly selected emitter locations. (b), (c) Speed-of-sound reconstructions with straight-ray tomography using optimally selected four emitters and all the emitters, respectively. (d), (e) Speed-of-sound reconstructions using finite-frequency tomography. We use optimally selected four emitters and all the emitters, respectively. Selected emitters are illustrated in the bottom-left corner. The circles indicate the relative positions of the 16 elements in the emitter array (white dots in Fig. 6), and the filled circles indicate the selected ones in each case. In all reconstructions we only show the ROI, and we indicate the RMSE in times of flight. The initial RMSE is 1.77×10^{-6} s.

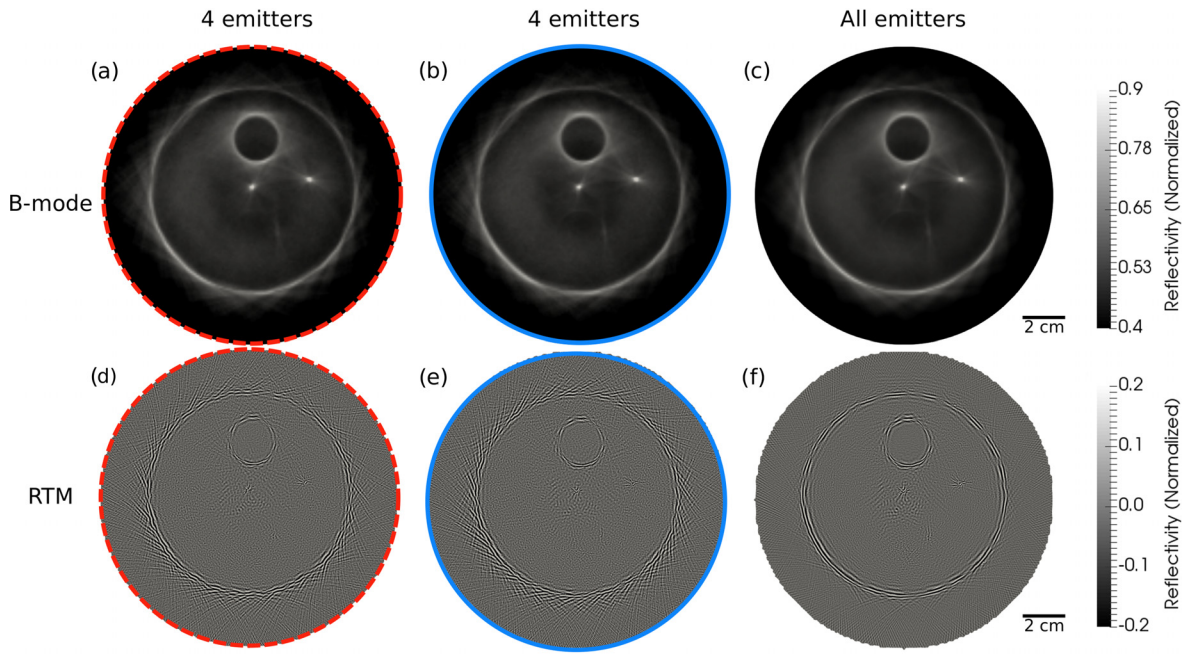

FIG. 8. (Color online) Reflectivity images using B-mode technique (top row) and RTM (bottom row). The emitter configurations used are: (left column) optimally selected 4 emitters jointly with straight-ray transmission; (middle column) 4 emitters jointly selected with finite-frequency transmission; and (right column) all emitters. Red dashed and blue solid circles indicate the background speed-of-sound models in Fig. 7 used for reflectivity imaging.

Because the emitter configuration is simultaneously optimized also for reflectivity imaging techniques, in Fig. 8 we show the images resulting from B-mode and RTM techniques. We use the spectral element solver Salvus (Afanasiev *et al.*, 2019) for the numerical wave propagation simulations required for RTM. Similar to the transmission case, there are no significant differences between the images obtained from 4 and 16 emitters. In all cases, the features resolved with the complete dataset are also recovered when using only 25% of the dataset. Here, we also validate the linearization assumptions made in the context of optimal experimental design. Although we select the most informative emitters assuming a homogeneous model in the estimation of the covariance operator, the reflectivity images are obtained using speed-of-sound reconstructions shown in Fig. 7.

VI. DISCUSSION AND CONCLUSION

In this study, we introduce the D-SOED method in the context of breast tissue imaging with ultrasound. Our approach is flexible enough to optimize the acquisition system for both transmission and reflection data, and using either ray-based or wave-based methods for the reconstructions. This flexibility is crucial for USCT, where the final product is a collection of images of different acoustic properties of the tissue. Although we only consider reflectivity and speed of sound, the extension to other properties, such as attenuation and density, is straightforward. The performance comparison for different imaging methods is beyond the scope of this work.

The concept of optimality, however, is ambiguous, and this can be observed, for instance, in the number of different optimality criteria available in the literature. This ambiguity is caused by the constraint of expressing with a scalar value the information contained in the covariance operator. Typically, one must choose which statistical properties will be emphasized at the expenses of the rest, and this selection depends on the aim of the experiment itself. In our case, we define the optimal experimental design through the D-optimality condition, which minimizes the volume of the joint confidence ellipsoid for the estimated parameters. Therefore, our results do not necessarily guarantee to improve other attributes, as for instance the inter-parameter trade-offs. A more integrating approach could be based on the combination of different optimality criteria (Curtis, 1999).

Additional constraints introduced in the optimal experimental design method also include the definition of the design parameters. Here, we choose to select the number and locations of the informative transducers, but other choices are also possible. To reduce the space of the possible experimental designs, we predefine some candidate values for the design parameters. This requires some prior information about the acquisition system, which typically is available. Examples of this are the approximate dimensions of the transducer holder or the frequencies of the emitted signal. Note that all these choices will affect the optimal design, which is important to keep in mind when interpreting the results. Under these constraints, however, the D-optimality condition has an important invariant property that makes our results general. Different model parameterizations yield same D-optimal designs. This is crucial when the parameterization is not fixed for post-acquisition reconstructions.

Although ideally the experimental design should be optimized prior to any realization of the experiment, we demonstrate that our approach can similarly be applied post-acquisition. In this way, the computational cost of the reconstructions can be controlled, and this has a significant impact in the context of clinical practice, where fast answers are

key. Similar approaches have recently been applied in geophysical exploration to reduce the large data volume in marine seismic surveys (Coles *et al.*, 2015). However, the redundancies identified by the D-SOED approach may also be used not just to reduce the dataset but as a complementary analysis for other methods. These could include, for example, the mini-batch (Boehm *et al.*, 2018) or source encoding (Wang *et al.*, 2014) approaches in the context of waveform tomography.

Finally, it is important to mention that, while the computational cost of D-SOED method may be challenging for large-scale problems, the benefit of an optimized USCT system, in terms of the image quality and computational resources, for clinical practice is tremendous. Once the acquisition system is optimized, the impact of the reduced cost in the recursive use of the scanning system may become very significant.

ACKNOWLEDGMENTS

The authors gratefully acknowledge Editor Bradley E. Treeby and two anonymous reviewers for the constructive comments that substantially improved the manuscript. We also thank Laura Ermert, Dirk-Philip van Herwaarden, and Sölvi Thrastarson for their valuable suggestions. The research leading to this study has received funding from the Swiss Commission for Technology and Innovation under Grant No. 17962.1 PFLS-LS. Furthermore, we gratefully acknowledge support by the Swiss National Supercomputing Centre (CSCS) under Project Grant No. d72.

[1]See supplementary material at https://doi.org/10.1121/1.5122291 for a comparison of reconstructions using 2, 3, and 4 optimally selected emitters.

Afanasiev, M., Boehm, C., van Driel, M., Krischer, L., Rietmann, M., May, D. A., Knepley, M. G., and Fichtner, A. (**2019**). "Modular and flexible spectral-element waveform modelling in two and three dimensions," Geophys. J. Int. **216**(3), 1675–1692.

Alexanderian, A., and Saibaba, A. (**2018**). "Efficient D-optimal design of experiments for infinite-dimensional Bayesian linear inverse problems," SIAM J. Sci. Comput. **40**(5), A2956–A2985.

André, M., Wiskin, J., and Borup, D. (**2013**). "Clinical results with ultrasound computed tomography of the breast," in *Quantitative Ultrasound in Soft Tissues*, edited by J. Mamou and M. L. Oelze (Springer Netherlands, Dordrecht), pp. 395–432.

Atkinson, A. C., and Donev, A. N. (**1992**). *Optimum Experimental Designs* (Oxford University Press, Oxford), pp. 1–344.

Attia, A., Alexanderian, A., and Saibaba, A. K. (**2018**). "Goal-oriented optimal design of experiments for large-scale Bayesian linear inverse problems," Inv. Probl. **34**(9), 095009.

Boehm, C., Korta Martiartu, N., Vinard, N., Balic, I. J., and Fichtner, A. (**2018**). "Time-domain spectral-element ultrasound waveform tomography using a stochastic quasi-Newton method," Proc. SPIE **10580**, 105800H.

Bozdag, E., Trampert, J., and Tromp, J. (**2011**). "Misfit functions for full waveform inversion based on instantaneous phase and envelope measurements," Geophys. J. Int. **185**(2), 845–870.

Bunks, C., Saleck, F. M., Zaleski, S., and Chavent, G. (**1995**). "Multiscale seismic waveform inversion," Geophysics **60**(5), 1457–1473.

Camacho, J., Medina, L., Cruza, J. F., Moreno, J. M., and Fritsch, C. (**2012**). "Multimodal ultrasonic imaging for breast cancer detection," Arch. Acoust. **37**(3), 253–260.

Claerbout, J. F. (**1971**). "Toward a unified theory of reflector mapping," Geophysics **36**(3), 467–481.

Coles, D., Prange, M., and Djikpesse, H. (**2015**). "Optimal survey design for big data," Geophysics **80**(3), P11–P22.

Curtis, A. (**1999**). "Optimal design of focused experiments and surveys," Geophys. J. Int. **139**(1), 205–215.

Curtis, A. (**2004**). "Theory of model-based geophysical survey and experimental design: Part 1—Linear Problems," Leading Edge **23**(10), 997–1004.

Curtis, A., Michelini, A., Leslie, D., and Lomax, A. (**2004**). "A deterministic algorithm for experimental design applied to tomographic and microseismic monitoring surveys," Geophys. J. Int. **157**(2), 595–606.

Dai, W., and Schuster, G. T. (**2013**). "Plane-wave least-squares reverse-time migration," Geophysics **78**(4), S165–S177.

Dapp, R., Zapf, M., and Ruiter, N. V. (**2011**). "Geometry-independent speed of sound reconstruction for 3D USCT using apriori information," in *2011 IEEE International Ultrasonics Symposium*, pp. 1403–1406.

Dette, H., and O'Brien, T. E. (**1999**). "Optimality criteria for regression models based on predicted variance," Biometrika **86**(1), 93–106.

Duric, N., Littrup, P., Li, C., Roy, O., Schmidt, S., Cheng, X., Seamans, J., Wallen, A., and Bey-Knight, L. (**2014**). "Breast imaging with SoftVue: Initial clinical evaluation," Proc. SPIE **9040**, 90400V.

Fichtner, A. (**2010**). *Full Seismic Waveform Modelling and Inversion* (Springer, Heidelberg), pp. 1–343.

Fichtner, A., Kennett, B. L. N., Igel, H., and Bunge, H. P. (**2008**). "Theoretical background for continental- and global-scale full-waveform inversion in the time-frequency domain," Geophys. J. Int. **175**(2), 665–685.

Gauthier, O., Virieux, J., and Tarantola, A. (**1986**). "Two-dimensional nonlinear inversion of seismic waveforms: Numerical results," Geophysics **51**(7), 1387–1403.

Gemmeke, H., Dapp, R., Hopp, T., Zapf, M., and Ruiter, N. V. (**2014**). "An improved 3D Ultrasound Computer Tomography system," in *2014 IEEE International Ultrasonics Symposium*, pp. 1009–1012.

Gemmeke, H., and Ruiter, N. (**2007**). "3D ultrasound computer tomography for medical imaging," Nucl. Instrum. Meth. Phys. Res. Sec. A: Accel. Spectrom. Detect. Assoc. Equip. **580**(2), 1057–1065.

Goncharsky, A., Romanov, S. Y., and Seryozhnikov, S. Y. (**2016**). "A computer simulation study of soft tissue characterization using low-frequancy ultrasonic tomography," Ultrasonics **67**, 136–150.

Greenleaf, J. F., Johnson, S. A., and Bahn, R. C. (**1977**). "Quantitative cross-sectional imaging of ultrasound parameters," in *1977 Ultrasonics Symposium*, pp. 989–995.

Guest, T., and Curtis, A. (**2009**). "Iteratively constructive sequential design of experiments and surveys with nonlinear parameter-data relationships," J. Geophys. Res.: Solid Earth **114**(B4), B04307, https://doi.org/10.1029/2008JB005948.

Hormati, A., Jovanović, I., Roy, O., and Vetterli, M. (**2010**). "Robust ultrasound travel-time tomography using the bent ray model," Proc. SPIE **7629**, 76290I.

Ihrig, A., and Schmitz, G. (**2018**). "Accelerating nonlinear speed of sound reconstructions using a randomized block Kaczmarz algorithm," in *2018 IEEE International Ultrasonics Symposium (IUS)*, pp. 1–9.

Jensen, T. L., Jørgensen, J. H., Hansen, P. C., and Jensen, S. H. (**2012**). "Implementation of an optimal first-order method for strongly convex total variation regularization," BIT Numer. Math. **52**(2), 329–356.

Johnson, S., Abbott, T., Bell, R., Berggren, M., Borup, D., Robinson, D., Wiskin, J., Olsen, S., and Hanover, B. (**2007**). "Non-invasive breast tissue characterization using ultrasound speed and attenuation," in *Acoustical Imaging*, edited by M. P. André (Springer Netherlands, Dordrecht), pp. 147–154.

Khodja, M. R., Prange, M. D., and Djikpesse, H. A. (**2010**). "Guided Bayesian optimal experimental design," Inv. Probl. **26**(5), 055008.

Korta Martiartu, N., Boehm, C., and Fichtner, A. (**2019**). "3D wave-equation-based finite-frequency tomography for ultrasound computed tomography," in press, available at https://arxiv.org/abs/1908.03302.

Korta Martiartu, N., Boehm, C., Vinard, N., Jovanović Balic, I., and Fichtner, A. (**2017**). "Optimal experimental design to position transducers in ultrasound breast imaging," Proc. SPIE **10139**, 101390M.

Lavarello, R., Kamalabadi, F., and O'Brien, W. D. (**2006**). "A regularized inverse approach to ultrasonic pulse-echo imaging," IEEE Trans. Med. Imag. **25**(6), 712–722.

Lavarello, R. J., and Hesford, A. J. (**2013**). "Methods for forward and inverse scattering in ultrasound tomography," in *Quantitative Ultrasound in Soft Tissues*, edited by J. Mamou and M. L. Oelze (Springer Netherlands, Dordrecht), pp. 345–394.

Li, C., Duric, N., Littrup, P., and Huang, L. (**2009**). "In vivo breast sound-speed imaging with ultrasound tomography," Ultrasound Med. Biol. **35**(10), 1615–1628.

Liu, C., Xue, C., Zhang, B., Zhang, G., and He, C. (**2018**). "The application of an ultrasound tomography algorithm in a novel ring 3D ultrasound imaging system," Sensors **18**(5), 1332.
Luo, Y., and Schuster, G. T. (**1991**). "Wave-equation traveltime inversion," Geophysics **56**(5), 645–653.
Marquering, H., Dahlen, F., and Nolet, G. (**1999**). "Three-dimensional sensitivity kernels for finite-frequency traveltimes: The banana-doughnut paradox," Geophys. J. Int. **137**(3), 805–815.
Matthews, T. P., Wang, K., Li, C., Duric, N., and Anastasio, M. A. (**2017**). "Regularized dual averaging image reconstruction for full-wave ultrasound computed tomography," IEEE Trans. Ultrason. Ferroelectr. Freq. Control **64**(5), 811–825.
Maurer, H., Curtis, A., and Boerner, D. E. (**2010**). "Recent advances in optimized survey design," Geophysics **75**(5), 75A177–75A194.
Maurer, H., Nuber, A., Korta Martiartu, N., Reiser, F., Boehm, C., Manukyan, E., Schmelzbach, C., and Fichtner, A. (**2017**). "Optimized experimental design in the context of seismic full waveform inversion and seismic waveform imaging," in *Advances in Geophysics*, edited by L. Nielsen (Elsevier, Amsterdam), Vol. 58, pp. 1–45.
Mercerat, E. D., and Nolet, G. (**2012**). "On the linearity of cross-correlation delay times in finite-frequency tomography," Geophys. J. Int. **192**(2), 681–687.
Mora, P. (**1989**). "Inversion = migration + tomography," Geophysics **54**(12), 1575–1586.
Ozmen, N., Dapp, R., Zapf, M., Gemmeke, H., Ruiter, N. V., and van Dongen, K. W. A. (**2015**). "Comparing different ultrasound imaging methods for breast cancer detection," IEEE Trans. Ultrasonics Ferroelectr. Freq. Control **62**(4), 637–646.
Pérez-Liva, M., Herraiz, J. L., Udías, J. M., Miller, E., Cox, B. T., and Treeby, B. E. (**2017**). "Time domain reconstruction of sound speed and attenuation in ultrasound computed tomography using full wave inversion," J. Acoust. Soc. Am. **141**(3), 1595–1604.
Pratt, R. G., Huang, L., Duric, N., and Littrup, P. (**2007**). "Sound-speed and attenuation imaging of breast tissue using waveform tomography of transmission ultrasound data," Proc. SPIE **6510**, 65104S.
Roy, O., Jovanović, I., Hormati, A., Parhizkar, R., and Vetterli, M. (**2010**). "Sound speed estimation using wave-based ultrasound tomography: Theory and GPU implementation," Proc. SPIE **7629**, 76290J.
Roy, O., Zuberi, M. A. H., Pratt, R. G., and Duric, N. (**2016**). "Ultrasound breast imaging using frequency domain reverse time migration," Proc. SPIE **9790**, 97900B.
Ruiter, N. V., Zapf, M., Hopp, T., Dapp, R., and Gemmeke, H. (**2012**). "Phantom image results of an optimized full 3D USCT," Proc. SPIE **8320**, 832005.
Ruiter, N. V., Zapf, M., Hopp, T., Gemmeke, H., and van Dongen, K. W. A. (**2017**). "USCT data challenge," Proc. SPIE **10139**, 101391N.
Ruiter, N. V., Zapf, M., Hopp, T., Gemmeke, H., van Dongen, K. W. A., Camacho, J., Herraiz, J. L., Liva, M. P., and Udías, J. M. (**2018**). "USCT reference data base: Conclusions from the first SPIE USCT data challenge and future directions," Proc. SPIE **10580**, 105800Q.
Sandhu, G. Y., Li, C., Roy, O., Schmidt, S., and Duric, N. (**2015**). "Frequency domain ultrasound waveform tomography: Breast imaging using a ring transducer," Phys. Med. Biol. **60**(14), 5381.
Sandhu, G. Y., West, E., Li, C., Roy, O., and Duric, N. (**2017**). "3D frequency-domain ultrasound waveform tomography breast imaging," Proc. SPIE **10139**, 1013909.
Schwarzenberg, G. F., Zapf, M., and Ruiter, N. V. (**2007**). "P3D-5 aperture optimization for 3D ultrasound computer tomography," in *2007 IEEE Ultrasonics Symposium Proceedings*, pp. 1820–1823.
Stavros, A. T., Thickman, D., Rapp, C. L., Dennis, M. A., Parker, S. H., and Sisney, G. A. (**1995**). "Solid breast nodules: Use of sonography to distinguish between benign and malignant lesions," Radiology **196**(1), 123–134.
Stotzka, R., Ruiter, N. V., Mueller, T. O., Liu, R., and Gemmeke, H. (**2005**). "High resolution image reconstruction in ultrasound computer tomography using deconvolution," Proc. SPIE **5750**, 315–326.
Tarantola, A. (**1984**). "Linearized inversion of seismic reflection data," Geophys. Prospect. **32**(6), 998–1015.
Tarantola, A. (**2005**). *Inverse Problem Theory and Methods for Model Parameter Estimation* (Society for Industrial and Applied Mathematics, Philadelphia), pp. 1–339.
Taskin, U., van der Neut, J., and van Dongen, K. W. A. (**2018**). "Redatuming for breast ultrasound," in *2018 IEEE International Ultrasonics Symposium (IUS)*, pp. 1–9.
Tromp, J., Tape, C., and Liu, Q. (**2005**). "Seismic tomography, adjoint methods, time reversal and banana-doughnut kernels," Geophys. J. Int. **160**(1), 195–216.
Vinard, N., Korta Martiartu, N., Boehm, C., Jovanović Balic, I., and Fichtner, A. (**2018**). "Optimized transducer configuration for ultrasound waveform tomography in breast cancer detection," Proc. SPIE **10580**, 105800I.
Wang, K., Matthews, T., Anis, F., Li, C., Duric, N., and Anastasio, M. A. (**2015**). "Waveform inversion with source encoding for breast sound speed reconstruction in ultrasound computed tomography," IEEE Trans. Ultrason. Ferroelectr. Freq. Contr. **62**, 475–493.
Warner, M., and Guasch, L. (**2016**). "Adaptive waveform inversion: Theory," Geophysics **81**(6), R429–R445.
Wiskin, J., Borup, D., Johnson, S., Andre, M., Greenleaf, J., Parisky, Y., and Klock, J. (**2013**). "Three-dimensional nonlinear inverse scattering: Quantitative transmission algorithms, refraction corrected reflection, scanner design and clinical results," Proc. Meetings Acoust. **19**(1), 075001.
Wiskin, J., Borup, D. T., Johnson, S. A., and Berggren, M. (**2012**). "Non-linear inverse scattering: High resolution quantitative breast tissue tomography," J. Acoust. Soc. Am. **131**(5), 3802–3813.
Zografos, G., Koulocheri, D., Liakou, P., Sofras, M., Hadjiagapis, S., Orme, M., and Marmarelis, V. (**2013**). "Novel technology of multimodal ultrasound tomography detects breast lesions," Eur. Rad. **23**(3), 673–683.